Scanning Kelvin Probe Force Microscopy and Density Functional Theory Studies on the Surface Potential of the Intermetallics in AA7075-T6 Alloys

Ni Li, Chaofang Dong, Xin Wei, Chen Man, Jizheng Yao, Jiangli Cao, and Xiaogang Li

The surface potentials of Mg_2Si and Al_7Cu_2Fe intermetallic particles in AA7075-T6 alloys were investigated by scanning Kelvin probe force microscopy (SKPFM) technique. The experimental surface potentials of Mg_2Si and Al_7Cu_2Fe intermetallic particles relative to Al matrix were ranging from -368 to -265 mV and 480–500 mV, respectively. A theoretical method for assessing relative nobility of intermetallics in Al alloys was discussed through first principle calculation. The work functions and surface energies of Mg_2Si and Al_7Cu_2Fe surfaces were calculated by using density functional theory (DFT) method. The results showed that work functions and surface energies of Mg_2Si and Al_7Cu_2Fe intermetallics were influenced by the orientations of crystal face and terminal types. At the oxygen coverage of 1/4 ML and 1 ML, the theoretical surface potential differences between Mg_2Si intermetallics and Al matrix were increased by 10–560 mV and 0–620 mV, while those between Al_7Cu_2Fe intermetallics and Al matrix were increased by 62–360 mV and 102–331 mV. For the adsorption of oxygen atom, theoretical surface potentials of Mg_2Si and Al_7Cu_2Fe intermetallics relative to Al matrix had a close agreement with the experimental surface potentials. It was verified that DFT method was a valuable theoretical approach to assess the relative nobility of different phases in alloys.

1. Introduction

Aluminum (Al) alloys are widely used in aerospace industry owing to the properties of low density, high strength and high stiffness. Various alloying elements such as Zn, Mg, Cu and Si were added into Al matrix to achieve high mechanical properties (Ref 1, 2). However, the intermetallic particles (IMPs), which were precipitated if the concentration of alloying elements reached a particular level, had a negative effect on corrosion resistance of Al alloys (Ref 3, 4). For example, pits were observed to initiate most commonly at the interface of intermetallics and Al matrix, due to micro-galvanic interactions (Ref 5). Previous studies found that such localized damaging might trigger other forms of localized corrosion, such as intergranular corrosion (Ref 6) and stress corrosion cracking (SCC) (Ref 7). Therefore, it is important to investigate the electrochemical behavior of intermetallics in Al alloys.

Ni Li, Chaofang Dong, Xin Wei, Chen Man, Jizheng Yao, Jiangli Cao, and **Xiaogang Li,** Corrosion and Protection Center, Key Laboratory for Corrosion and Protection (MOE), University of Science and Technology Beijing, Beijing 100083, People's Republic of China. Contact e-mail: cfdong@ustb.edu.cn.

The related surface potential (ψ) was the measurable quantity characterizing electrochemical behavior of a metal surface. The scan Kelvin probe force microscopy (SKPFM) was a technique that allowed detection of surface potential of the examined surface relative to the Kelvin probe tip (Ref 8). Schmutz and Frankel measured the contact surface potentials of several pure metals by SKPFM technology in the air. They found a linear correlation between surface potential measured in nominally dry air and free corrosion potential upon the immersed specimens (Ref 9). SKPFM technique had been widely applied in addressing the problem of corrosion of alloys (Ref 10, 11). However, the lateral resolution of SKPFM only reached 100 nm in ambient air (Ref 12). Ralston found that the second phases with a critical width of 8 nm could behave as electrochemical entities in aggressive electrolyte solution (Ref 13). Therefore, prediction of the surface potentials of extremely small phases without using SKPFM technique still remained a challenge.

To overcome the shortcomings of SKPFM technique, a density functional theory (DFT) calculation was introduced to understand the surface physical properties and the nobility of intermetallics relative to matrix. Ying Jin et al. (Ref 14) calculated the theoretical surface potentials of Al_2Cu, Mg_2Si, Al_2CuMg and $MgZn_2$ intermetallics relative to Al matrix, which had a general agreement with experimental surface potentials. The surfaces of those four intermetallics were clean and unoxidized, whereas oxide films were covered on the surfaces of real alloy during experiments.

In this paper, we investigated two precipitations in AA7075-T6 alloy, which were Mg_2Si and Al_7Cu_2Fe intermetallics with micrometers size. The surface properties of Mg_2Si and Al_7Cu_2Fe intermetallics with different orientations of crystal face and terminal elements were analyzed by work functions and surface energies. The theoretical surface potentials of the

intermetallics relative to Al matrix with oxygen adsorption were calculated by the values of electron work functions. We found that the theoretical surface potential differences had a close agreement with the experimental surface potential differences. It was verified that the first principle calculation was an effective way for assessing relative nobility of phases in alloys.

2. Experimental and Computational Details

2.1 Computation Details

In this study, the work functions of the intermetallics were calculated by the Medea-VASP 5.4 software on the basis of DFT plane-wave method (Ref 15). The exchange–correlation functional for describing the interactions was the generalized gradient approximation of Perdew–Burke–Ernzerhof (GGA-PBE) (Ref 16). All calculations were performed using 600 eV user-defined cutoff energy. In this paper, stoichiometric slab models were adopted consisting of more than 6–8 atomic layers to calculate the work functions and surface energies of the surfaces. The lower halves of the slab models were fixed, whereas the upper halves were allowed to relax. The electronic iteration convergence was set as 1.00×10^{-5} eV by using the Normal (blocked Davidson) algorithm. A 15 Å vacuum layer between surfaces was included to prevent interactions between the upper surface and lower surface. The convergence criterion for the slab structure optimization was set for 0.02 eV/Å. Stoichiometric slab models of Mg_2Si and Al_7Cu_2Fe intermetallics, which were usually dissymmetric, were adopted in this study. Thus, dipole correction was performed to eliminate the artificial electric field caused by different terminations.

2.1.1 Work Function and Surface Energy. Work function and surface energy are the basic parameters in surface physics. Surface energy is the energy required to split an infinite crystal to two parts, i.e., the amount of energy of a crystal required for the formation of a new surface (Ref 17). However, experimental determination of surface energy was difficult (Ref 18). The theoretical surface energy (γ_{surf}) can be calculated by the following equation (Ref 17, 19):

$$\gamma_{surf} = (E_{total} - NE_{bulk})/2A \qquad \text{(Eq 1)}$$

where E_{total} is the total VASP energy of the slab model, N is the number of total atoms, E_{bulk} is the energy per atom in the bulk, and A is the area of the surface.

Work function was defined as the minimum work required for extracting an electron from the bulk of material through surface to a point outside the sample (Ref 8). The work function ϕ for a given surface was defined as follows (Ref 8, 20):

$$\phi = -e\varphi - E_F = -\mu_e + e\chi \qquad \text{(Eq 2)}$$

where e is the charge of an electron, φ is the electrostatic potential in the vacuum nearby the surface, and E_F is the Fermi level inside the surface. The work function (ϕ) comprises the chemical work (μ_e) and the electrostatic work to transport the charged electron through the dipole layer of the surface ($e\chi$). χ is the dipole or surface potential, which is significantly influenced by orientations of crystal face.

2.1.2 Surface Potential Difference. SKPFM is a technique that measures the surface potentials of the studied surfaces relative to the Kelvin probe tip. The surface potentials of the intermetallics relative to the probe tip ($\psi_{intermetallics}^{tip}$), and the surface potentials of the aluminum matrix relative to the probe tip (ψ_{matrix}^{tip}) measured by SKPFM can be described as followed (Ref 8):

$$\psi_{Intermetallics}^{tip} = \frac{\phi_{tip} - \phi_{intermetallics}}{e} \qquad \text{(Eq 3)}$$

$$\psi_{matrix}^{tip} = \frac{\phi_{tip} - \phi_{matrix}}{e} \qquad \text{(Eq 4)}$$

Thus, the surface potential difference between intermetallics and the matrix ($\psi_{matrix}^{intermetallics}$) can be obtained from Eq 3 and 4:

$$\psi_{matrix}^{intermetallics} = \frac{\phi_{intermetallics} - \phi_{matrix}}{e} \qquad \text{(Eq 5)}$$

According to Eq 5, the theoretical surface potential differences between intermetallics and Al matrix can be obtained by calculating the work function of intermetallics ($\phi_{intermetallics}$) and matrix (ϕ_{matrix}) by the DFT method. If $\psi_{matrix}^{intermetallics} < 0$, the intermetallics are considered to be more active than the matrix. If $\psi_{matrix}^{intermetallics} > 0$, the intermetallics appear nobler than the matrix.

2.2 Experiments

The material investigated was AA7075-T6 aluminum alloy with the chemical composition (wt.%) Al-6.2Zn-2.7Mg-1.56Cu-0.23Fe-0.08Si. Disk samples (Φ12 mm, 2 mm thick) were cut from the AA7075-T6 sheet. Diamond polishing agent and alcohol were used during surface preparation (grinding and polishing). The disk specimens were mechanically ground progressively by hand using 600, 800, 1200, 2000, 3000, 5000 grit SiC grinding papers, and polished with 2 and 1 μm diamond paste. The specimen was immersed into neutral 0.1 M NaCl solution at room temperature for various durations, then cleaned in distilled water, dried in air and transferred into SKPFM for measurements at room temperature. Based on our observations, a immersion time of about 5 min, 30 min, 120 min was selected.

Mg_2Si and Al_7Cu_2Fe intermetallics in AA7075-T6 alloy were identified by using a scanning electron microscope (SEM; FEI Quanta250) equipped with an energy dispersive spectrometer (EDS) and having the ability to generate backscattered electron Kikuchi patterns (BEKPs) for combined chemical and structural phase identification. The accelerating voltage is 15 kV. The SKPFM measurements were performed on an atomic force microscopy (Multimode VIII, Bruker). To map the surface potential, SKPFM was performed by a PFQNE-AL probe with a silicon tip on a silicon nitride cantilever. The morphology image was obtained by AFM scanning with the tapping mode in which the tip contacted with the sample surface. The potential mapping was got in the second scanning with a lift height of 60 nm, so it can eliminate the effect of morphology. All of images in this work were obtained at a scanning rate of 0.45 Hz with a resolution of 512 × 512, and the intermetallics were marked with the help of a Vickers.
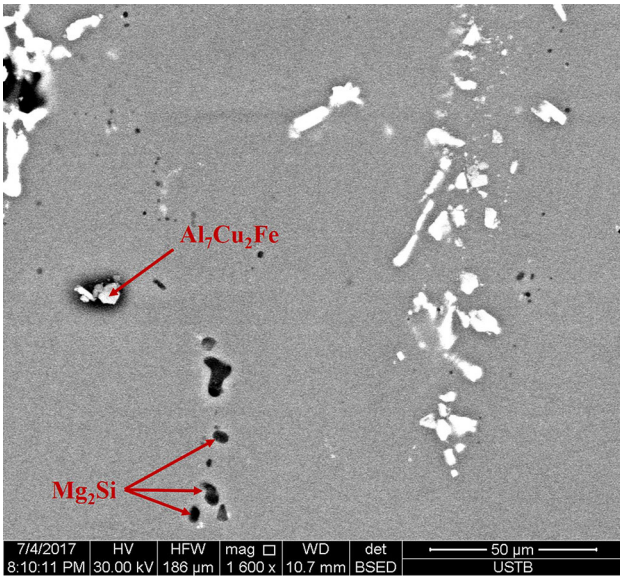
Fig. 1 Backscattered electron image of the mechanically polished surface in AA7075 alloy

3. Results and Discussion

3.1 Microstructural Analysis

A mechanically polished specimen of the AA7075-T6 alloy was examined by SEM/EDS to determine the distribution and composition of intermetallics. Figure 1 shows the microstructure of AA7075-T6 viewed with an SEM (in backscattered electron mode), indicating the existence of constituent type particles. The light particles were (Al, Cu, Fe, Si, Mn) constituent particles, which include Al_7Cu_2Fe, Al_2Cu, Al_3Fe, Al-Fe-Si and so on, and the three dark particles were Mg_2Si phases through the EDS analysis. We note that strengthening

Table 1   EDS analysis of Mg_2Si and Al_7Cu_2Fe

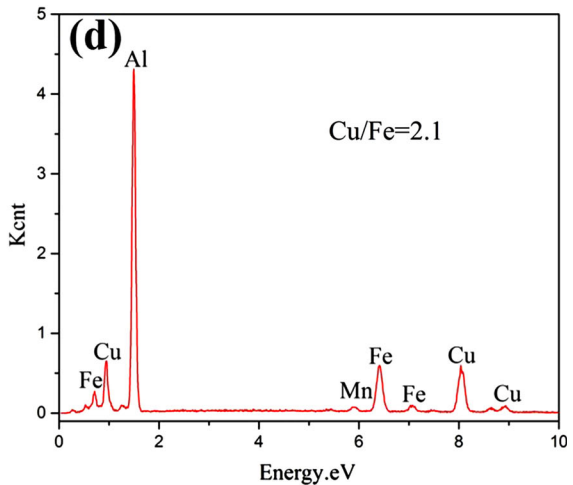| Intermetallics	Composition, at.%					
	Al	Mg	Cu	Si	Fe	Zn
Mg_2Si	68.27	18.48	0	10.07	0	2.41
Al_7Cu_2Fe	76.84	1.5	13.39	0	6.41	1.1

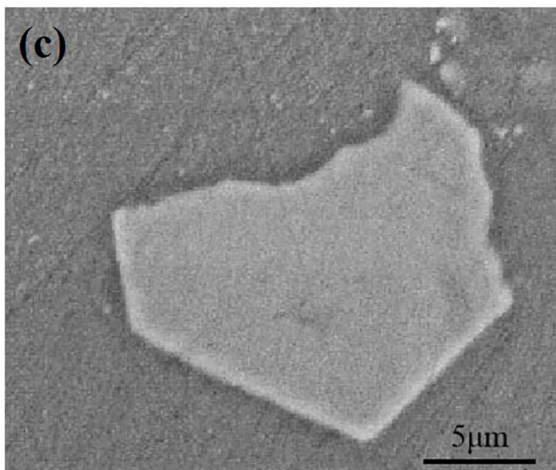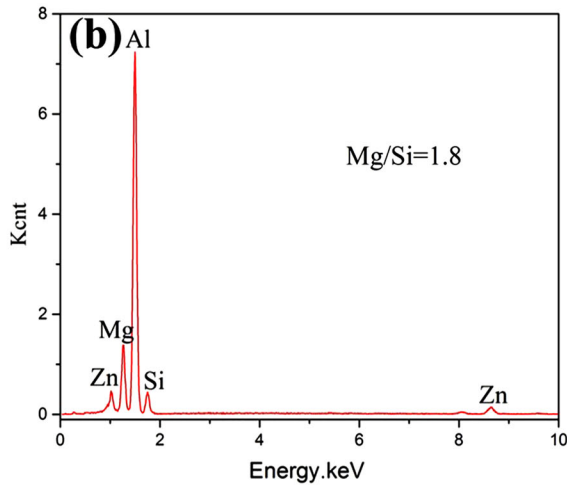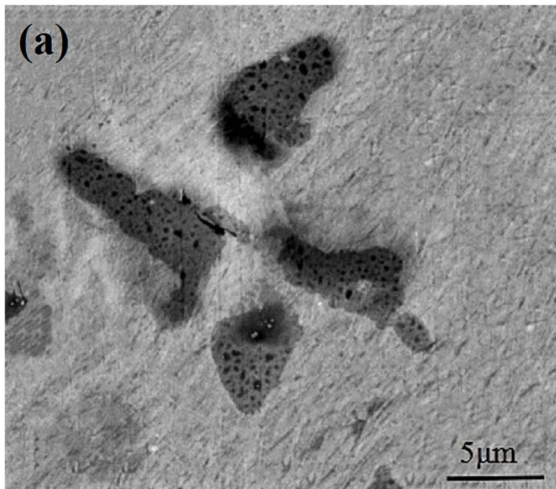**Fig. 2** Backscattered electron image and EDS spectrum of (a), (b) Mg_2Si and (c), (d) Al_7Cu_2Fe intermetallics

sub-micron MgZn$_2$ (η) phase presented at a high number density was not resolved with SEM. In this study, we investigated Mg$_2$Si and Al$_7$Cu$_2$Fe phases, which exhibited different electrochemical properties in AA7075-T6. As shown in Fig. 1, the size of Mg$_2$Si particles in AA7075-T6 alloy is in the range of 1–10 μm. These particles are characterized by a high Mg/Si atomic ratio, which ranges between 1.6 and 2.4. The size of Al$_7$Cu$_2$Fe particles is typically in the range of 1–20 μm. The Cu/Fe atomic ratio of these particles is 1.7-2.3.

The backscattered electron images of Fig. 2(a) and (c) displayed Mg$_2$Si and Al$_7$Cu$_2$Fe particles, which were identified by EDS analysis, respectively (Fig. 2b and d, Table 1). The Mg$_2$Si phase contained about at 68% of aluminum due to quite deep area from which x-ray is detected in EDS. The size of the Mg$_2$Si particles ranged between 4 and 10 μm, while the size of Al$_7$Cu$_2$Fe phase was about 15 μm. As shown in Table 1, Mg/Si atomic ratio of the Mg$_2$Si phase was 1.8, and Cu/Fe atomic ratio of the Al$_7$Cu$_2$Fe phase was 2.1.

3.2 SKPFM

As shown in Fig. 3(a) and (c), the surface potential of Mg$_2$Si particle was 368 mV lower than the surface potential of Al matrix, indicating that the Mg$_2$Si particle was active than the Al matrix. The surface potential differences between Mg$_2$Si intermetallics and the surrounding matrix ranged from − 368 to − 265 mV. As shown in Fig. 3(b) and (d), the surface potential of an Al$_7$Cu$_2$Fe particle was 500 mV higher than the surface potential of the Al matrix, which indicated that the Al$_7$Cu$_2$Fe particle was noble than the Al matrix. The surface potential differences between the Al$_7$Cu$_2$Fe intermetallics and Al matrix ranged between 480 and 500 mV.

Figure 4 shows the topography of the Mg$_2$Si intermetallics after polishing and immersion in 0.1 M NaCl solution for 5 min by AFM technique. As shown in Fig. 4(a) and (c), the Mg$_2$Si intermetallics were approximately the same height as Al matrix after polishing. As shown in Fig. 4(b), Mg$_2$Si particles were dissolved quickly and the corrosion products deposited on the surface around the Mg$_2$Si particles after immersion in 0.1 M NaCl for 5 min. The depth of the pit on Mg$_2$Si particle was 75 nm (Fig. 4d). The average corrosion rate of the Mg2Si particle was 15 nm/min. With the increase in the immersion time, the corrosion rate decreased. For example, after immersion in 0.1 M NaCl for 30 min and 120 min, the depth of the pit was, respectively, 115 and 125 nm, as shown in Fig. 4(e) and (f). The average corrosion rate was 3.83 and 1.04 nm/min. With the prolongation of immersion time, the pits still maintained their localized form despite of some growth in depth and stopped growing after immersion in 0.1 M NaCl solution for 2 h. For Al$_7$Cu$_2$Fe particle, no pit was observed after 120 min immersion.

The dissolution of Mg$_2$Si intermetallics was associated with the chemical process and anodic electrochemical activity (Ref 21). At the initial stage, Mg$_2$Si was hydrolyzed by water
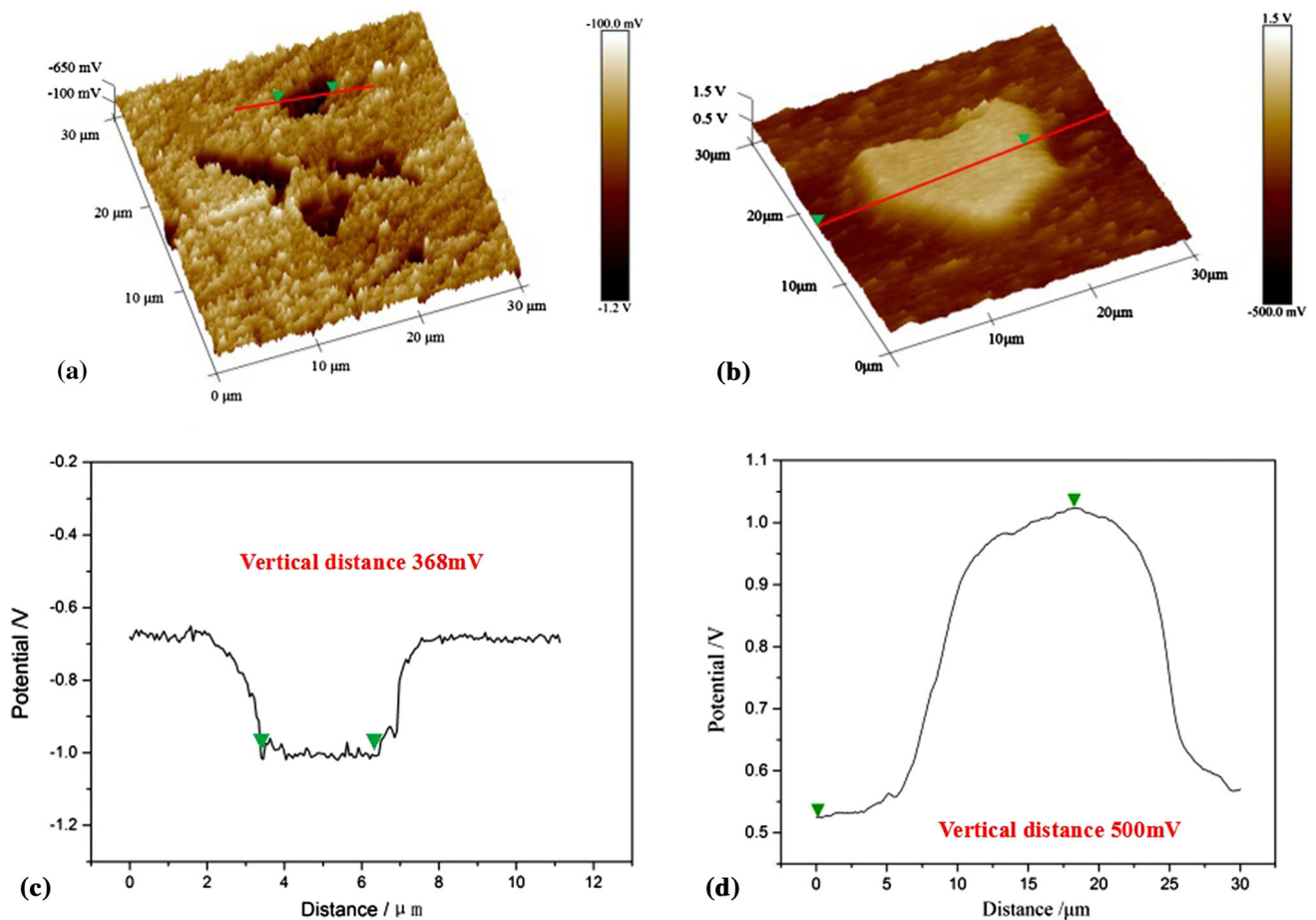

Fig. 3 SKPFM potential map and section analysis of (a), (c) Mg$_2$Si and (b), (d) Al$_7$Cu$_2$Fe in AA7075-T6
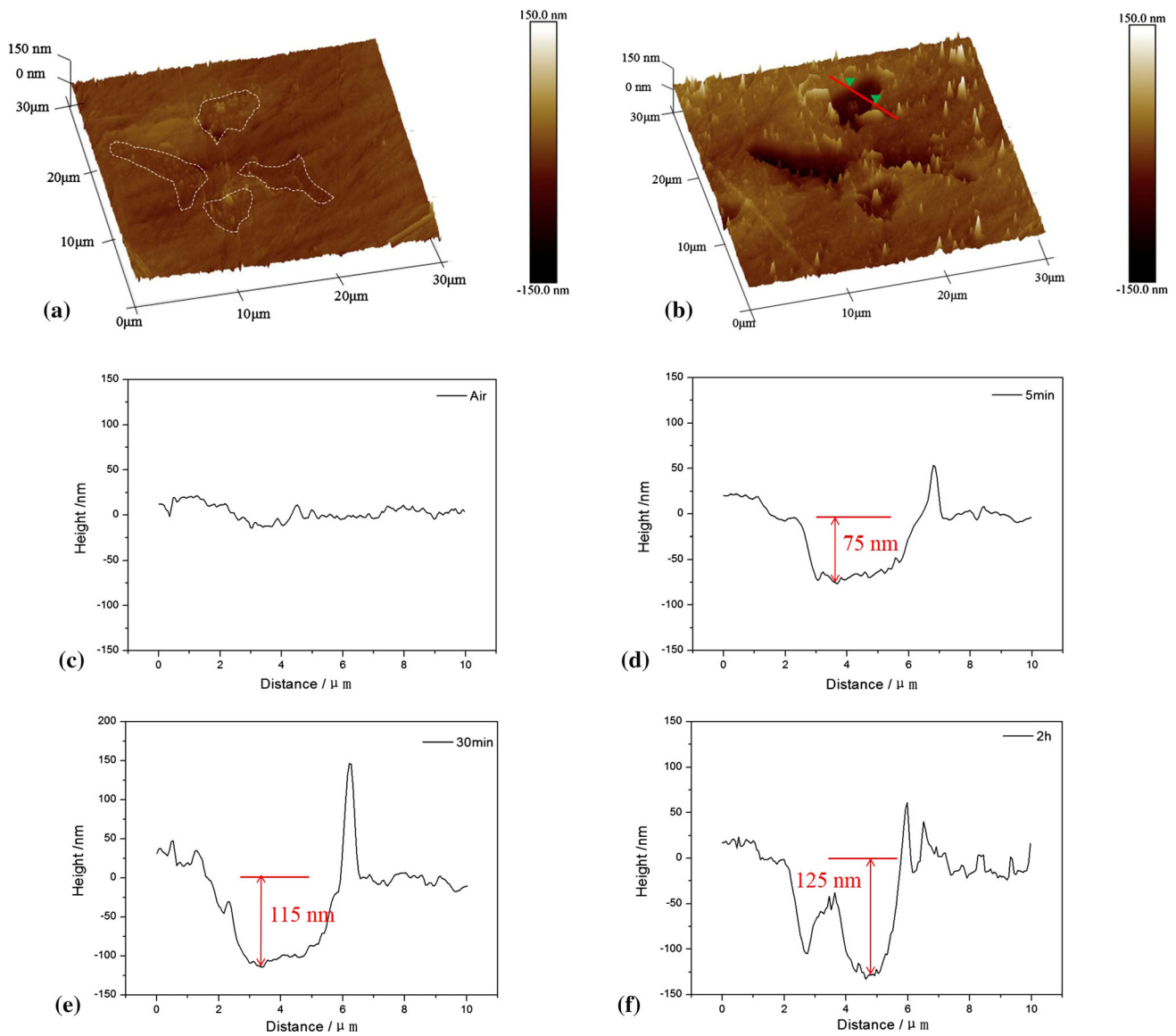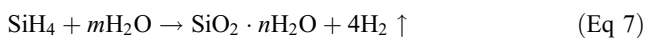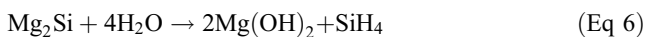
Fig. 4 AFM topography and section analysis of Mg$_2$Si intermetallics after (a) (c) polishing, (b) (d) after immersion in 0.1 M NaCl for 5 min, (e) after immersion in 0.1 M NaCl for 30 min and (f) after immersion in 0.1 M NaCl for 120 min

resulting in the formation of different types of silanes (in Eq 6); hydrolysis of silane occurred releasing H$_2$ and formed silicon hydroxides on the surface of Mg$_2$Si particle (in Eq 7); the electrochemical dissolution of Mg from the Mg$_2$Si intermetallic particles could occur resulting in Si and SiO$_2$ enrichments due to the anodic characterization of Mg$_2$Si (in Eq 8).

$$Mg_2Si + 4H_2O \rightarrow 2Mg(OH)_2 + SiH_4 \qquad (Eq\ 6)$$

$$SiH_4 + mH_2O \rightarrow SiO_2 \cdot nH_2O + 4H_2 \uparrow \qquad (Eq\ 7)$$

$$Mg_2Si + 2H_2O \rightarrow 2Mg^{2+} + SiO_2 + 4H^+ + 8e^- \qquad (Eq\ 8)$$

As shown in Fig. 5(a), the Mg$_2$Si particle presented 368 mV lower surface potentials than the Al matrix by SKPFM measurement before immersion. After immersion in 0.1 M NaCl solution for 5 min, the surface potentials of Mg$_2$Si particles became 316 mV higher than that of Al matrix in Fig. 5(b) and (d). The surface potential was ranged from − 0.65 to − 0.99 V. After immersion in 0.1 M NaCl solution

for 30 min and 120 min, the surface potential was ranged from − 0.92 to − 0.59 mV and − 0.75 to − 0.31 mV, as shown in Fig. 5(e) and (f). It was seen that the surface potential of Mg$_2$Si particles and Al matrix were both increasing with prolongation of the immersion time due to the corrosion products deposited on the surfaces. As shown in Fig. 5(d), (e) and (f), the surface potential difference increased with extending the immersion time, because the increasing rate of the surface potential on Mg$_2$Si particle was higher than that on Al matrix. The inversion of electrochemical nobility also occurred on the surface of Al$_2$CuMg phase after immersion in corroded solution (Ref 5). As shown in Fig. 6, after immersion in 0.1 M NaCl for 5 min, the content of the Al and Mg elements was decreased, while the content of Si was unchanged. The reason is that the active elements such as Mg and Al (anodic) tend to dissolve into solution resulting in Si (cathodic) enrichment (Ref 5, 22). The Si enrichment (SiO$_2$ and SiO$_2$·nH$_2$O) deposited on the surface of the pits prevented the Mg$_2$Si particles from dissolution further. Decrease in magnesium content was accompanied by appearance of an oxygen peak resulting from formation of
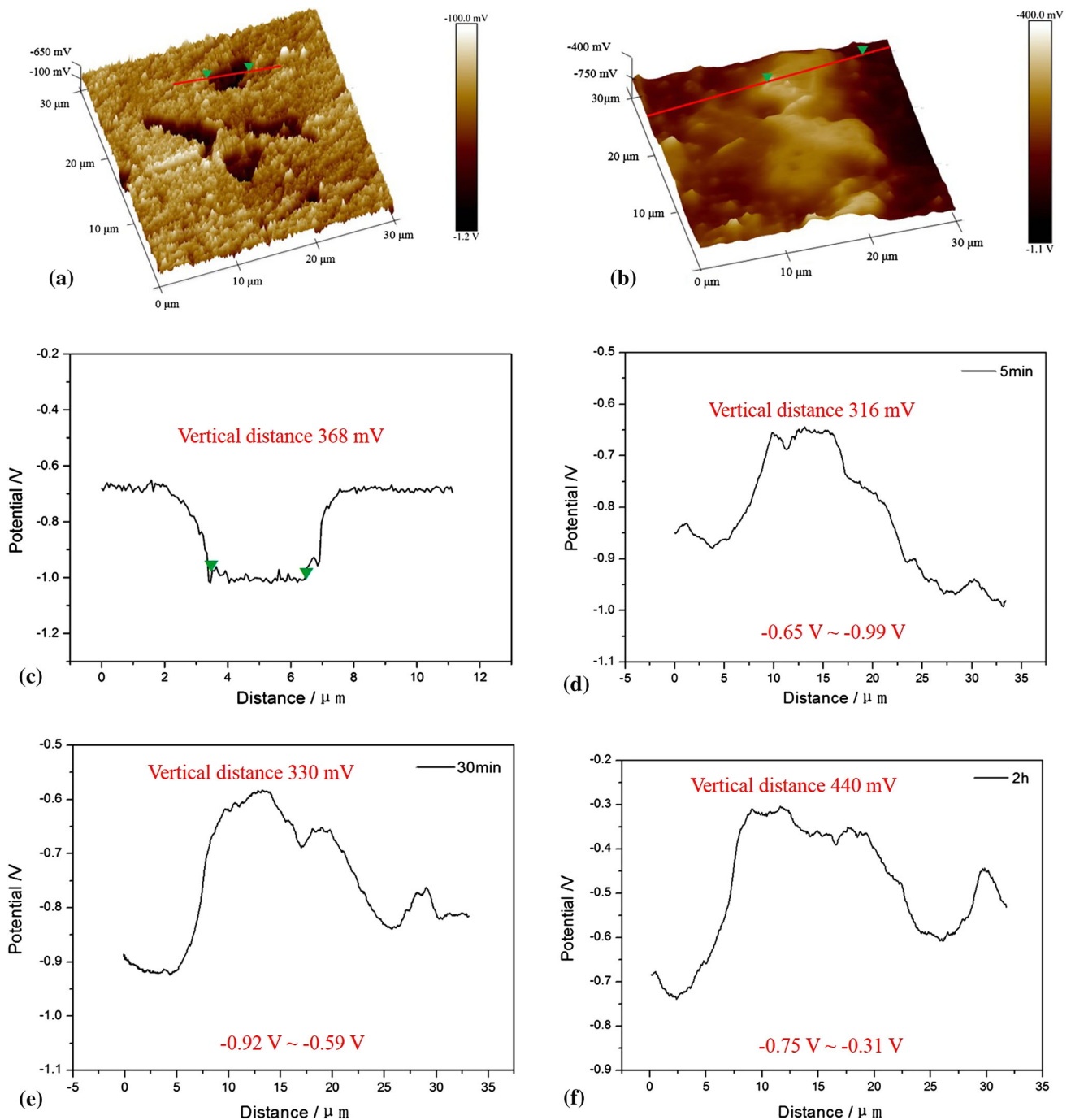
Fig. 5 Surface potential map for Mg$_2$Si phase (a), (c) before immersion, and (b), (d) after immersion in 0.1 M NaCl for 5 min

oxide or hydroxide compounds. The formation of the hydroxide (Mg(OH)$_2$) deposited on the top of Mg$_2$Si was the most likely reason for relatively low corrosion activity of this phase. That is why the corrosion rate decreased with the prolongation of the immersion time.

3.3 Work Function and Surface Energy

3.3.1 Pure Metals. Surface energy and work function are the two basic quantities in surface physics. There were numerous studies focusing on calculating the surface energy and work function via the DFT method (Ref 17, 23). Mg$_2$Si

consisted of Mg and Si elements, and Al$_7$Cu$_2$Fe was composed of three metal elements—Al, Cu and Fe. The calculated results in this work and experimental results in previous studies of the work functions and surface energies of these pure metals are listed in Table 2.

To estimate the accuracy of our results, the calculated work functions and surface energies were compared with experimental results shown in Table 2. It was clearly seen that the values of surface energies and work functions calculated by GGA-PBE method are in close agreement with those obtained in experiments (Ref 17, 23-26). The surface energies and work functions were anisotropic and dependent on the orientations of

crystal face. For pure Al, (100) surface was with the lowest surface energy, indicating that it was the most stable surface exposed to air. (111) plane with the smallest work function was the easiest orientation to lose electrons. Figure 7 shows the average work functions and surface energies of Mg, Al, Fe, Cu and Si surfaces. The average work functions and surface energies of Mg, Al, Fe, Cu and Si surfaces are obtained from the low index planes such as (100), (110), (111) surfaces, which are listed in Table 2. The surface energies of these metal surfaces increased according to the following order: $\gamma_{surf}^{Mg} < \gamma_{surf}^{Al} < \gamma_{surf}^{Cu} < \gamma_{surf}^{Si} < \gamma_{surf}^{Fe}$. The work functions for these pure metal surfaces increased based on the following order: $\phi_{Mg} < \phi_{Al} < \phi_{Fe} < \phi_{Cu} < \phi_{Si}$.

3.3.2 Mg$_2$Si and Al$_7$Cu$_2$Fe. The models of Mg$_2$Si, Al$_7$Cu$_2$Fe phases are shown in Fig. 8. Mg$_2$Si phase had cubic symmetry with space group Fm3 m, and Al$_7$Cu$_2$Fe phase had tetragonal symmetry with space group P4/mnc. The optimized
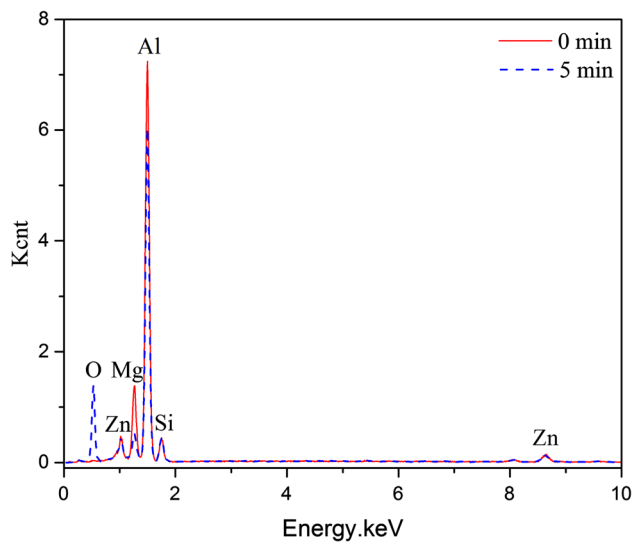
lattice constants of these phases, which were close to the experimental values (Ref 28, 29), are listed in Table 3. The discrepancies were less than 3‰, indicating that the parameters and structures adopted in our calculation could provide sufficiently precise results.

To construct the structural models of the low index surfaces of Mg$_2$Si, we considered six different possible surfaces: (100), (110), (111), (120), (112), (122), as shown in Fig. 9. The mix (Mg, Si)-terminated surfaces were more stable than Si- or Mg-terminated surfaces because of the small surface energies as illustrated in Table 4. The work functions of Mg$_2$Si surfaces ranged between 3.33 and 4.81 eV with different orientations of crystal face. The work function of (100) surface was the largest, indicating that the (100) face was the noblest. For Mg$_2$Si (111) plane, the work functions of Mg-terminated surfaces (3.33 and 4.03 eV) are smaller than that of Si-terminated surfaces (4.44 eV). The results prove that the work function and surface energy of Mg$_2$Si surfaces were influenced by the orientations of crystal face and terminal elements. At the oxygen coverage of 1/4 ML, the work functions were increased by 0.08 –1.22 eV, which indicated that Mg$_2$Si surfaces turn to be nobler. It is because the O atoms absorbed on the surfaces could capture the electrons of the surfaces. For Mg$_2$Si (111) plane, the work functions of Mg-terminated surfaces (4.28 and 4.55 eV) were smaller than that of Si-terminated surfaces (4.91 eV) with the oxygen adsorption. When the oxygen coverage increased to 1 ML, the work functions were raised by 0.17–1.31 eV. For (100), (111) and (120) surface, the work functions of Si-terminated surfaces were larger than that of Mg-terminated surfaces. It was also found that the orientations of crystal face and the terminal elements had an effect on the work functions of Mg$_2$Si surfaces with oxygen coverage.

Since Al$_7$Cu$_2$Fe contained three elements which had a complicated structure, Al$_7$Cu$_2$Fe surfaces had various terminations shown in Fig. 10. The work functions and surface energies of (100), (110), (001) surfaces were calculated, which are listed in Table 5. The surface energies of the Al$_7$Cu$_2$Fe surfaces ranged from 1.41 to 1.96 J/m^2 along various orientations of crystal face and terminal elements. For Al$_7$Cu$_2$Fe (100) face, the work function of the Cu-terminated surface (4.43 eV) was larger than that of Al-terminated surface (4.08 eV),

Fig. 6 EDS spectrum of Mg$_2$Si particle before and after immersion in 0.1 M NaCl for 5 min

Table 2 Work functions (ϕ) and surfaces energy (γ_{surf}) of surfaces along different orientations of pure metals

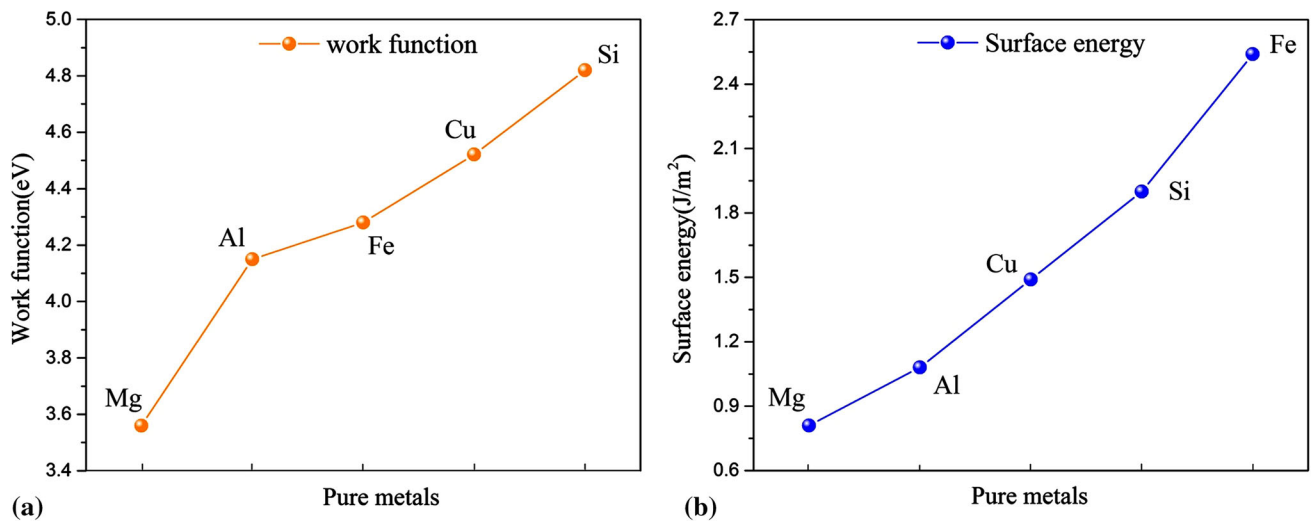| Metals | Surface | ϕ, eV | | γ_{surf}, J/m^2 | |
		Calculated	Experimental	Calculated	Experimental
Mg	(100)	3.636	3.66 (Ref 17)	0.61	0.79 (Ref 17)
	(110)	3.542		0.76	
	(111)	3.61		0.72	
Al	(110)	4.13	4.06 ± 0.03 (Ref 24)	0.96	1.14 (Ref 24)
	(111)	4.05	4.26 ± 0.03 (Ref 24)	1.35	
	(100)	4.28	4.20 ± 0.03 (Ref 24)	0.92	
Fe	(100)	3.89	4.31 (Ref 25)	2.54	2.48 (Ref 25)
	(110)	4.72		2.50	
	(111)	3.927		2.36	
Cu	(100)	4.45	4.59 (Ref 26)	1.30	1.79 (Ref 26)
	(110)	4.43	4.48 (Ref 26)	1.35	
	(111)	4.68	4.94 (Ref 26)	1.83	
Si	(100)	5.38	4.49 ± 0.05 (Ref 27)	2.00	
	(111)	4.48	4.71 ± 0.05 (Ref 27)	2.20	
	(110)	4.725		1.77	

Fig. 7 The work functions (a) and the surface energies (b) of pure metals
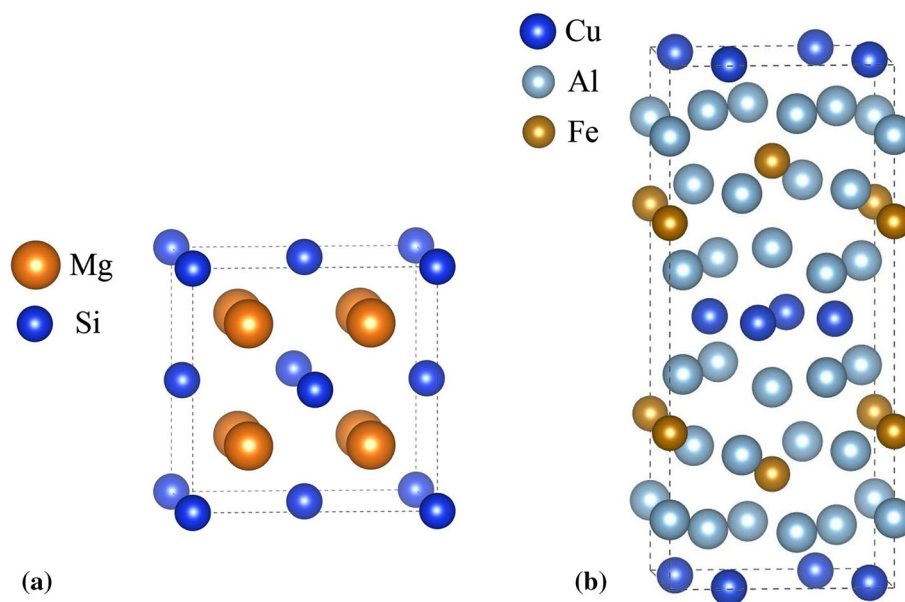
Fig. 8 Schematic drawing of crystal structure: Mg$_2$Si (a), Al$_7$Cu$_2$Fe (b)

Table 3 Lattice parameters of the Mg$_2$Si and Al$_7$Cu$_2$Fe phases

Phases	Mg$_2$Si		Al$_7$Cu$_2$Fe	
	Cal.	Exp. (Ref 28)	Cal.	Exp. (Ref 29)
Cryst. Sys.	Cubic		Tetragonal	
Space group	Fm-3 m		P4/mnc	
A	6.358 Å	6.370 Å	6.331 Å	6.336 Å
B	6.358 Å	6.370 Å	6.331 Å	6.336 Å
C	6.358 Å	6.370 Å	14.765 Å	14.87 Å

indicating that the work function was related to the terminal elements of outermost layer. There were seven kinds of terminations of (001) surface, i.e., Fe-Al-Fe, Fe-Al-Al, Al-Al-Cu, Al-Cu-Al, Al-Al-Fe, Al-Fe-Al and Cu-Al-Al (the left most layer represents the outermost layer). The corresponding work functions were 4.45, 4.14, 4.33, 4.32, 4.25, 4.04 and 4.29 eV, respectively. The work function of Al-Fe-Al-terminated surface was smaller than that of Al-Cu-Al-terminated surface, which indicated that the work function of Al$_7$Cu$_2$Fe surface was affected by the atomic type of sub-outermost layer. The work function of Fe-Al-Fe-terminated surface was larger than that of Fe-Al-Al-terminated surface. It demonstrated that atomic type of the third outermost layer still had an impact on the work function of Al$_7$Cu$_2$Fe surface. At the oxygen coverage of 1/4 ML, the work functions of Al$_7$Cu$_2$Fe phase were increased by 0.02–1.04 eV. When the oxygen coverage increased to 1 ML, the work functions were raised by 0.09–1.06 eV. The surfaces of Al$_7$Cu$_2$Fe became nobler induced by the adsorption of oxygen atom.
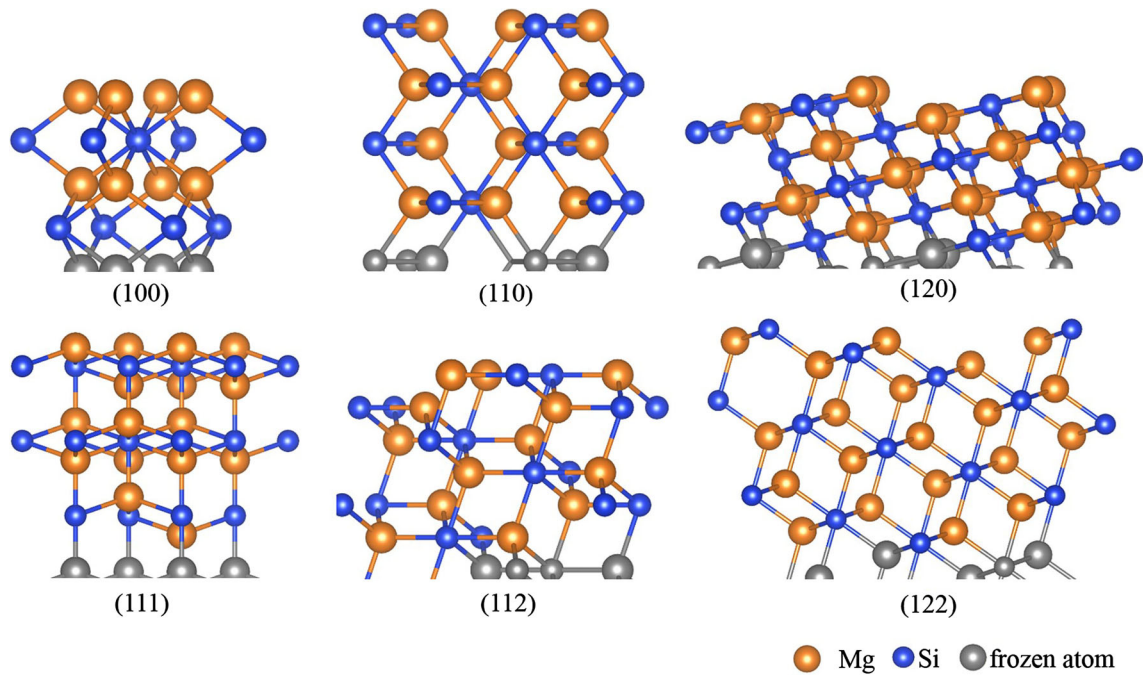
Mg   Si   frozen atom

Fig. 9 Atomic structure for various crystal face orientations of Mg$_2$Si

Table 4 The surface energy (γ_{surf}), the electron work function (ϕ) of Mg$_2$Si surfaces and the electron work function of Mg$_2$Si surfaces at the oxygen coverage of 1/4 ML ($\phi_{1/4}^O$) and 1 ML (ϕ_1^O)

Surfaces	Terminated plane	γ_{surf} , J/m^2	ϕ , eV	$\phi_{1/4}^O$, eV	ϕ_1^O , eV
(100)	Mg	1.49	4.27	4.39	4.45
	Si$_1$	1.47	4.81	4.89	5.02
	Si$_2$	1.47	4.55	4.91	5.00
(110)	Mix(Mg, Si)	0.783	3.94	4.57	4.60
(111)	Mg$_1$	2.13	3.33	4.55	4.64
	Si	3.64	4.44	4.91	5.12
	Mg$_2$	4.42	4.03	4.28	4.41
(120)	Mg	2.18	3.86	4.16	4.16
	Si	1.19	4.18	4.53	4.55
(122)	Mix(Mg, Si)	1.04	4.03	4.13	4.20
(112)	Mix(Mg, Si)	1.02	3.77	3.94	4.16

3.4 Surface Potential Difference

The theoretical values of surface potential difference between Al matrix and the phases were calculated according to Eq 5. The calculation results are presented in Table 6. In this study, we considered that the work function of Al matrix was approximately equal to that of pure Al. This assumption was reasonable because there was a precipitation free zone (PFZ) around the intermetallic particle and most of the alloying elements were concentrated in the secondary phases. The galvanic interaction was between the intermetallic particles and PFZ. As shown in Fig. 7(a), the average work function of pure Al was 4.15 eV. The presence of oxidation states might be contributing to the observed experimental results. However, the oxide films covered on the Mg$_2$Si and Al$_7$Cu2Fe particles were complex structures (Ref 30). The oxygen adsorption which was the first step for oxidation was investigated by first principle

calculation. The average work functions of pure Al with the 1/4 ML and 1 ML oxygen coverage were 4.24 and 4.32 eV.

As shown in Fig. 11, the theoretical surface potential difference between the two intermetallics and Al matrix increased with the adsorption of O atoms. At the oxygen coverage of 1/4 ML and 1 ML, the calculated values of surface potential differences between Mg$_2$Si intermetallics and Al matrix were increased by 10–560 mV and 0–620 mV, while the surface potential differences between Al$_7$Cu$_2$Fe intermetallics and Al matrix were increased by 62–360 mV and 102–331 mV. With the increase in oxygen coverage, the surface potential differences between intermetallics and Al matrix turn to be a relatively stable value. The experimental surface potential differences including the data in previous studies (Ref 31, 32) and those measured in this work are presented in Fig. 11 with different color regions. The calculated surface potential differences between the Mg$_2$Si phase and the Al matrix were
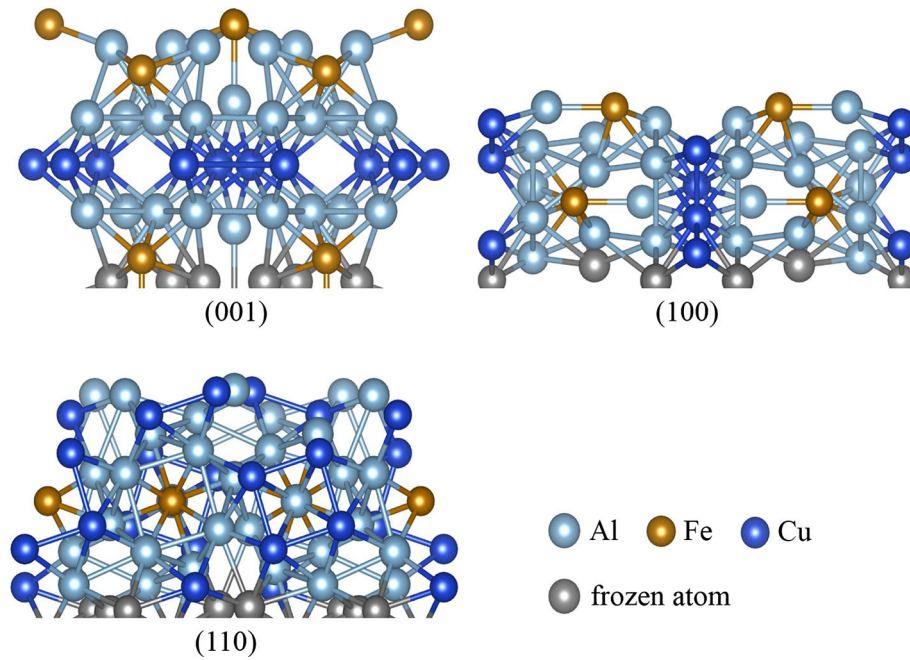
Fig. 10 Atomic structure of surfaces along different orientations in Al$_7$Cu$_2$Fe phase

Table 5 Surface energies (γ_{surf}), electron work functions (ϕ) of Al$_7$Cu$_2$Fe surfaces and electron work functions of Al$_7$Cu$_2$Fe surfaces at the O coverage of 1/4 ML ($\phi_{1/4}^O$) and 1 ML (ϕ_1^O)

Surface	Terminated plane	γ_{surf} , J/m^2	ϕ , eV	$\phi_{1/4}^O$, eV	ϕ_1^O , eV
(100)	Mix(Al, Fe)	1.71	4.34	4.51	4.72
	Mix(Al, Cu)	1.68	4.30	4.43	4.56
	Al	1.59	4.08	4.24	4.32
	Cu	1.65	4.43	4.58	4.65
(110)	Mix(Al, Cu)	1.85	4.25	4.53	4.72
	Mix(Al, Fe)	1.81	4.28	4.69	4.78
(001)	Fe-Al-Fe	1.68	4.45	5.15	5.22
	Al-Fe-Al	1.92	4.04	4.06	4.13
	Fe-Al-Al	1.96	4.14	5.18	5.20
	Al-Al-Cu	1.86	4.33	4.65	4.79
	Al-Cu-Al	1.54	4.32	4.78	4.82
	Cu-Al-Al	1.54	4.29	4.60	4.63
	Al-Al-Fe	1.48	4.25	4.59	4.61

Table 6 The calculated values of surface potential differences between the intermetallics and the Al matrix

	Mg$_2$Si			Al$_7$Cu$_2$Fe			
		$\psi_{matrix}^{Mg_2Si}$ (-O)/mV				$\psi_{matrix}^{Al_7Cu_2Fe}$ (-O)/mV	
Surface	$\psi_{matrix}^{Mg_2Si}$/mV	1/4 ML	1 ML	surface	$\psi_{matrix}^{Al_7Cu_2Fe}$ /mV	1/4 ML	1 ML
(100)	393	490	500	(100)	138	200	240
(110)	− 210	330	280				
(111)	− 220	340	400	(110)	115	370	430
(120)	− 130	110	100				
(122)	− 120	− 110	− 120	(001)	120	480	451
(112)	− 380	− 300	− 160				

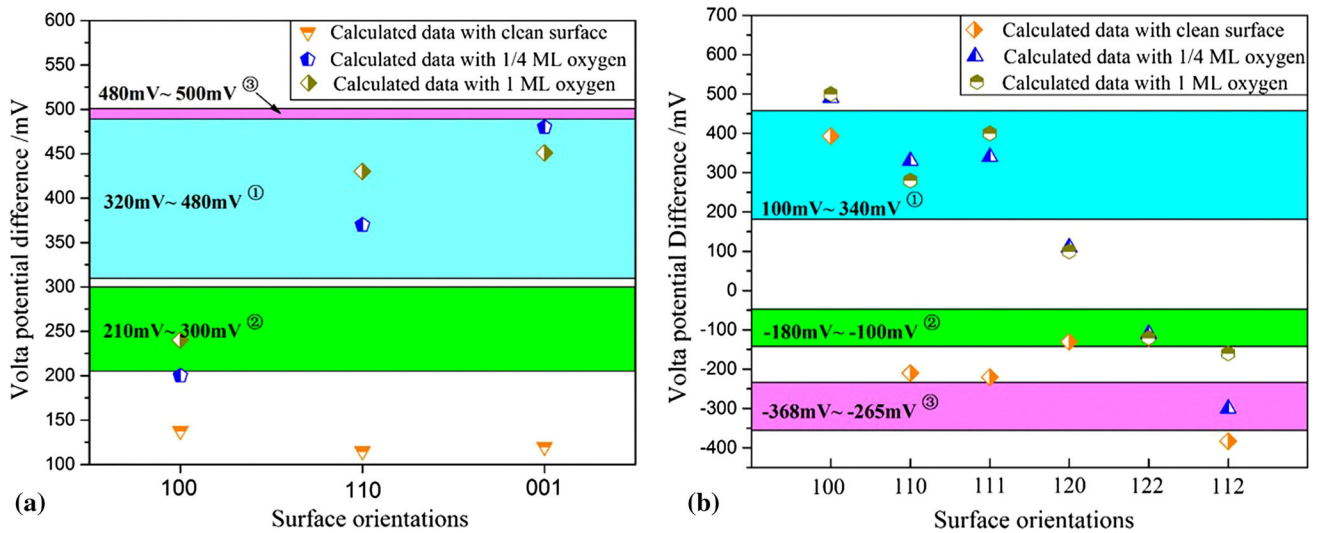**Fig. 11** The calculated surface potential of clean surfaces and O-adsorbed surfaces of (a) Al₇Cu₂Fe, (b) Mg₂Si relative to Al matrix; (①. Experimental, Ref [30]; ②. Experimental, Ref [31]; ③. This work)
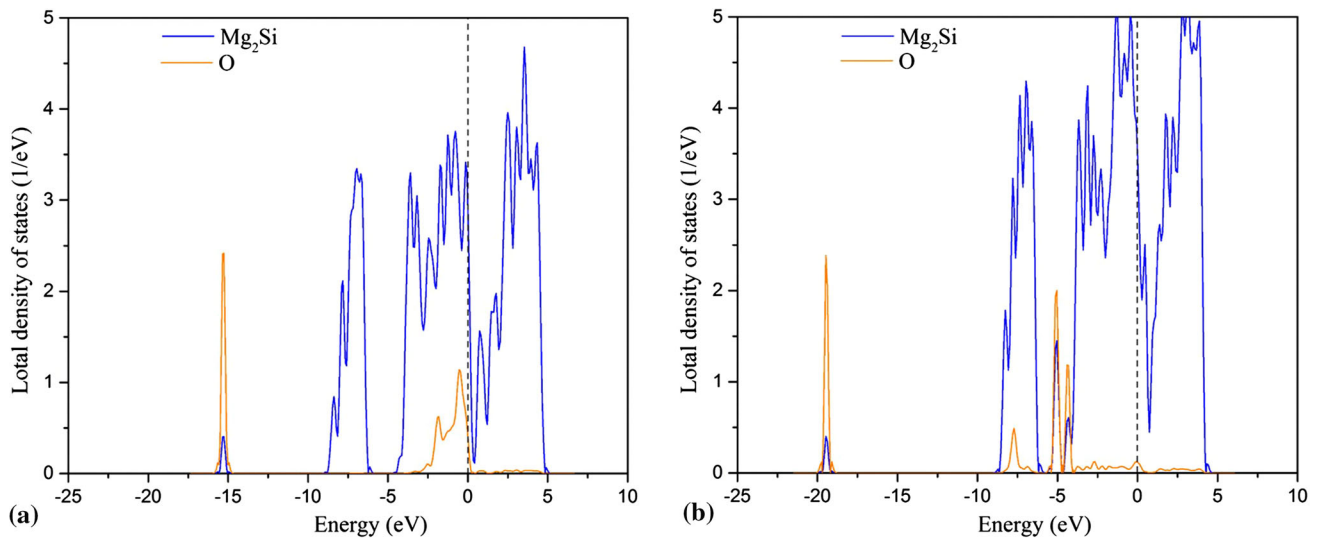

Fig. 12 LDOS for (a) Mg2Si (110) surface and (b) Mg2Si (122) surface with 1/4 ML oxygen: Mg2Si phase contributes in solid blue line and adsorbed O ion contributes in solid orange line (Color figure online)

negative in the absence of oxygen except for (100) surface, indicating that (100) surface was nobler than Al matrix (in Fig. 11b). The electrochemical behavior of (110), (111), (120) surfaces of Mg₂Si phase was changed from anodic to cathodic due to adsorption of O atom, whereas (122) and (112) surfaces still acted as anodic site relative to Al matrix. It is because the O atoms absorbed on different surfaces had different ability to capture electrons. According to Bader density analysis, the average charge transfer from Mg₂Si (110) surface to absorbed O atoms was 1.63, which was larger than that of 1.47 from (122) surface to absorbed O atoms at the oxygen coverage of 1/4 ML.

To investigate the interaction between O atoms and Mg₂Si-(110), Mg₂Si-(122) surfaces, we studied local density of state (LDOS) of the surfaces shown in Fig. 12. It could be found that

a peak of the LDOS for the O atoms absorbed on Mg₂Si-(110) surface occurred between the energies of − 15 to − 14 eV and − 3.8 to − 0.3 eV. It overlapped with a peak of the LDOS for Mg₂Si (110) surface, indicating atomic orbital hybridization between O atoms and the surface, shown in Fig. 12a. In comparison with LDOS of Mg₂Si (110) surface, the interaction between O atoms and Mg₂Si (122) surface was weaker due to the narrow peak range to share the energy shown in Fig. 12b.

The calculated surface potentials of Al₇Cu₂Fe phase relative to Al matrix are positive as shown in Fig. 11(a). The theoretical surface potential differences of clean Al₇Cu₂Fe surfaces were smaller than the experimental values. It was found that the theoretical surface potential differences essentially agreed with the experimental values, when the adsorption of O atoms was considered. Thus, oxide film played an important role in surface

potential and DFT calculation was an effective way to obtain surface potentials of intermetallics with different surface terminations and orientations of crystal faces.

4. Conclusion

The surface potentials of Mg_2Si and Al_7Cu_2Fe intermetallics were investigated by SKPFM technique. The work functions, surface energies and surface potentials of the Mg_2Si and Al_7Cu_2Fe intermetallics calculated by DFT method had been carefully analyzed in the paper. The main conclusions were summarized:

(1) The work functions and surface energies of the Mg_2Si and Al_7Cu_2Fe surfaces were related to the orientations of crystal face and the species of the terminated element. Mg-terminated surfaces were with lower work function than Si-terminated surfaces. Mix (Mg, Si)-terminated surface was more stable than Mg-terminated and Si-terminated surface from the point of surface energy.

(2) With the increase in oxygen coverage, the theoretical surface potential differences between the intermetallics and Al matrix turn to be a relatively stable value.

(3) The experimental surface potential difference between the Mg_2Si particle and Al matrix in our work was ranging from -368 to -265 mV, while the surface potential difference between Al_7Cu_2Fe and Al matrix ranged from 480 to 500 mV.

(4) For the adsorption of oxygen atoms, theoretical surface potential differences between the intermetallics and Al matrix were in accordance with the experimental values (in Fig. 10), which demonstrated that DFT method was an effective approach for prediction the relative nobility of intermetallics in alloys.

References

1. X. Yuan, K. Gao, G.S. Rohrer, and X. Fang, Grain Boundary Plane Distributions in a Hot Rolled 5A06 Aluminum Alloy, *Adv. Eng. Mater.*, 2014, **16**(9), p 1105–1110
2. R. Rana, R. Purohit, and S. Das, Reviews on the Influences of Alloying Elements on the Microstructure and Mechanical Properties of Aluminum Alloys and Aluminum Alloy Composites, *Int. J. Sci. Res. Publ.*, 2012, **2**(6), p 1–7
3. Y. Liu and Y. Cheng, Role of Second Phase Particles in Pitting Corrosion of 3003 Al Alloy in NaCl Solution, *Mater. Corros.*, 2010, **61**(3), p 211–217
4. J. Li, N. Birbilis, and R.G. Buchheit, Electrochemical Assessment of Interfacial Characteristics of Intermetallic Phases Present in Aluminium Alloy 2024-T3, *Corros. Sci.*, 2015, **101**, p 155–164
5. P. Leblanc and G. Frankel, A Study of Corrosion and Pitting Initiation of AA2024-T3 Using Atomic Force Microscopy, *J. Electrochem. Soc.*, 2002, **149**(6), p B239–B247
6. S. Jain, J. Hudson, and J. Scully, Effects of Constituent Particles and Sensitization on Surface Spreading of Intergranular Corrosion on a Sensitized AA5083 Alloy, *Electrochim. Acta*, 2013, **108**, p 253–264
7. D. Najjar, T. Magnin, and T. Warner, Influence of Critical Surface Defects and Localized Competition Between Anodic Dissolution and Hydrogen Effects During Stress Corrosion Cracking of a 7050 Aluminium Alloy, *Mater. Sci. Eng. A*, 1997, **238**(2), p 293–302
8. M. Rohwerder and F. Turcu, High-Resolution Kelvin Probe Microscopy in Corrosion Science: Scanning Kelvin Probe Force microscopy (SKPFM) Versus Classical Scanning Kelvin Probe (SKP), *Electrochim. Acta*, 2007, **53**(2), p 290–299
9. P. Schmutz and G. Frankel, Corrosion Study of AA2024-T3 by Scanning Kelvin Probe Force Microscopy and In Situ Atomic Force Microscopy Scratching, *J. Electrochem. Soc.*, 1998, **145**(7), p 2295–2306
10. V. Guillaumin, P. Schmutz, and G. Frankel, Characterization of Corrosion Interfaces by the Scanning Kelvin Probe Force Microscopy Technique, *J. Electrochem. Soc.*, 2001, **148**(5), p B163–B173
11. M. Iannuzzi, K. Vasanth, and G. Frankel, Unusual Correlation Between SKPFM and Corrosion of Nickel Aluminum Bronzes, *J. Electrochem. Soc.*, 2017, **164**(9), p C488–C497
12. N. Sathirachinda, R. Pettersson, S. Wessman, and J. Pan, Study of Nobility of Chromium Nitrides in Isothermally Aged Duplex Stainless Steels by Using SKPFM and SEM/EDS, *Corros. Sci.*, 2010, **52**(1), p 179–186
13. K. Ralston, N. Birbilis, M. Cavanaugh, M. Weyland, B. Muddle, and R. Marceau, Role of Nanostructure in Pitting of Al-Cu-Mg Alloys, *Electrochim. Acta*, 2010, **55**(27), p 7834–7842
14. Y. Jin, M. Liu, C. Zhang, C. Leygraf, L. Wen, and J. Pan, First-Principle Calculation of Volta Potential of Intermetallic Particles in Aluminum Alloys and Practical Implications, *J. Electrochem. Soc.*, 2017, **164**(9), p C465–C473
15. G. Kresse and J. Furthmüller, Efficient Iterative Schemes for Ab Initio Total-Energy Calculations Using a Plane-Wave Basis Set, *Phys. Rev. B*, 1996, **54**(16), p 11169
16. X. Wei, C. Dong, Z. Chen, K. Xiao, and X. Li, A DFT Study of the Adsorption of O_2 and H_2O on Al (111) Surfaces, *RSC Adv.*, 2016, **6**(61), p 56303–56312
17. J. Wang and S.-Q. Wang, Surface Energy and Work Function of fcc and bcc Crystals: Density Functional Study, *Surf. Sci.*, 2014, **630**, p 216–224
18. W. Tyson and W. Miller, Surface Free Energies of Solid Metals: Estimation from Liquid Surface Tension Measurements, *Surf. Sci.*, 1977, **62**(1), p 267–276
19. X. Tian, T. Wang, L. Fan, Y. Wang, H. Lu, and Y. Mu, A DFT Based Method for Calculating the Surface Energies of Asymmetric MoP Facets, *Appl. Surf. Sci.*, 2018, **427**, p 357–362
20. W. Li and D. Li, Effect of Surface Geometrical Configurations Induced by Microcracks on the Electron Work Function, *Acta Mater.*, 2005, **53**(14), p 3871–3878
21. K.A. Yasakau, M.L. Zheludkevich, S.V. Lamaka, and M.G. Ferreira, Role of Intermetallic Phases in Localized Corrosion of AA5083, *Electrochim. Acta*, 2007, **52**(27), p 7651–7659
22. L. Li, B. Zhang, B. Tian, Y. Zhou, J. Wang, E. Han, and W. Ke, SVET Study of Galvanic Corrosion of Al/Mg2Si Couple in Aqueous Solutions at Different pH, *J. Electrochem. Soc.*, 2017, **164**(6), p C240–C249
23. D.-P. Ji, Q. Zhu, and S.-Q. Wang, Detailed First-Principles Studies on Surface Energy and Work Function of Hexagonal Metals, *Surf. Sci.*, 2016, **651**, p 137–146
24. Z.-J. Zhao, A. Genest, and N. Rösch, Identification of Surface Species by Vibrational Normal Mode Analysis. A DFT Study, *Surf. Sci.*, 2017, **664**, p 233–240
25. H. Kobayashi and S. Kato, Observations on the Photoelectric Work Function and Leed Pattern from the (111) Surface of an Iron Single Crystal, *Surf. Sci.*, 1969, **18**(2), p 341–349
26. H.L. Skriver and N. Rosengaard, Surface Energy and Work Function of Elemental Metals, *Phys. Rev. B*, 1992, **46**(11), p 7157
27. R. Eastment and C. Mee, Work Function Measurements on (100) (110) and (111) Surfaces of Aluminium, *J. Phys. F Metals Phys.*, 1973, **3**(9), p 1738
28. C. Nakhowong, T. Sumpao, and T. Seetawan, Synthesis and Characterization of Mg_2Si Thermoelectric Material, *Advanced Materials*

Research, J. Nukeaw and W. Pecharapa, Eds., Trans Tech Publications, 2013, p 213–217

29. J. Proveti, C. Larica, and E. Passamani, Structural Properties and Phase Transformation in Mechanically Alloyed Al/Cu/Fe System, *J. Phys. D Appl. Phys.*, 2003, **36**(7), p 798

30. J. Ryl, J. Wysocka, M. Jarzynka, A. Zielinski, J. Orlikowski, and K. Darowicki, Effect of Native Air-Formed Oxidation on the Corrosion Behavior of AA 7075 Aluminum Alloys, *Corros. Sci.*, 2014, **87**, p 150–155

31. F. Andreatta, H. Terryn, and J. De Wit, Effect of Solution Heat Treatment on Galvanic Coupling Between Intermetallics and Matrix in AA7075-T6, *Corros. Sci.*, 2003, **45**(8), p 1733–1746

32. J. De Wit, Local Potential Measurements with the SKPFM on Aluminium Alloys, *Electrochim. Acta*, 2004, **49**(17–18), p 2841–2850